JOURNAL OF AIRCRAFT
Vol. 32, No. 3, May–June 1995

Numerical Investigation of High Incidence Flow over a Double-Delta Wing

J. A. Ekaterinaris* and R. L. Coutley†
Naval Postgraduate School, Monterey, California 93943
Lewis B. Schiff‡
NASA Ames Research Center, Moffett Field, California 94035
and
M. F. Platzer§
Naval Postgraduate School, Monterey, California 93943

The vortical flowfield over a double-delta wing configuration, consisting of a sharp leading-edge 76-deg sweep strake and a 40-deg sweep wing section is investigated numerically. The governing equations are solved with a partially upwind, finite difference, two-factor algorithm. The leeward-side vortex system resulting from the strake and wing vortices is investigated for a subsonic freestream speed of $M_\infty = 0.22$, high Reynolds number turbulent flow at various angles of incidence. At low angles of attack the strake and wing vortices remain separate over the wing section, whereas for flows at higher angles of attack the two vortices merge and vortex breakdown develops. Vortex breakdown appears initially in the trailing-edge region of the wing section. As the angle of attack increases, bursting occurs further upstream closer to the strake section. The effect of numerical grid density is investigated, and the solutions are compared with available experimental data. The computed surface pressures are in good agreement with the experimental measurements for the lower angles of attack, but the agreement deteriorates as the angle of attack increases.

Introduction

INVESTIGATION of the vortical flowfield over delta wings in large incidence subsonic flow is an active area of current theoretical and experimental research. The main feature of the flow over a delta wing at an angle of attack is the leeward-side vortical flowfield resulting from the separation of the windward- and leeward-side boundary layers from the leading edge. The separated boundary layers spiral over the wing leeward side to form vortex cores. In the leeward-side leading-edge vortices the flow significantly accelerates and strong flow gradients are developed. This energetic character of the leeward-side vortical flowfield provides nonlinear lift that has been successfully utilized on modern aircraft. As the angle of attack increases, the leeward-side leading-edge vortices are strengthened, and the lift of the delta wing increases until a critical angle of attack is reached, where bursting of the vortices occurs and the structure of the flowfield changes dramatically. Downstream of the bursting point reversed axial velocities are usually observed, and the breakdown is followed by a turbulent wake. Breakdown has adverse effects on the lift characteristics and may cause self-excited oscillatory motion and buffeting. Understanding the mechanisms that generate vortex breakdown, and the ability to predict its occurrence, is crucial to efforts to improve current aircraft design and performance in flight at high angle of attack.

Due to its fundamental and applied importance, the phenomenon of vortex breakdown has been studied both experimentally and theoretically. Experimental studies of vortex breakdown have investigated axisymmetric swirling flows confined in cylindrical tubes as well as flows over delta wings. Various forms of vortex breakdown occurring in axisymmetric tube swirling flows are described in Ref. 1. Among these forms only bubble- and spiral-type vortex breakdowns were observed for flows over delta wings, depending on the angle of attack and the wing aspect ratio. The bubble form is characterized by a stagnation point that is located on the leading-edge vortex swirl axis, followed by an abrupt expansion of the vortex core to form an envelope of a bubble of recirculating fluid. The spiral type of vortex breakdown, on the other hand, is characterized by a rapid deceleration of the fluid along the leading-edge vortex swirl axis and formation of an abrupt kink. The whole spiral structure rotates in a periodic fashion about the swirl axis opposite to the direction of the flow in the leading-edge vortex. More recently, continuing interest in defining the structure of the vortical flowfield and the effect of vortex breakdown on flows over delta and double-delta wings has led to several experimental investigations.[2–6] Various flow regimes, ranging from low speed to transonic flow were investigated. Delta wings having varying aspect ratios were examined, and both bubble and spiral vortex breakdown was identified depending on the angle of attack and the aspect ratio.

The flow over single-delta wings and double-delta wings was also studied recently by numerical solution of the Navier-Stokes equations.[7–10] The results of these numerical investigations were in good agreement with the experimental measurements, and both bubble- and spiral-type breakdown were identified. The present work focuses on the investigation of the flowfield over a strake-wing configuration in high Reynolds number subsonic flow. In previous numerical works different configurations have been considered, and mainly the laminar flow regime for lower Reynolds number flows over

Presented as Paper 91-0753 at the AIAA 29th Aerospace Sciences Meeting and Exhibit, Reno, NV, Jan. 7–10, 1991; received Sept. 14, 1993; revision received Aug. 4, 1994; accepted for publication Aug. 8, 1994.

*Research Associate Professor, Navy-NASA Joint Institute for Aeronautics. Senior Member AIAA.
†Graduate Student, Department of Aeronautics and Astronautics; currently at Air Test Center, Patuxent River, MD.
‡Special Assistant for High Alpha Technology, Fluid Dynamics Division. Associate Fellow AIAA.
§Professor, Department of Aeronautics and Astronautics. Associate Fellow AIAA.

delta wings has been investigated. The main feature of the flow over the double-delta wing is the presence of both the strake and wing vortices. At low angles of incidence the strake and wing vortices remain distinct and only weak interaction is observed. The strong interaction between the strake and wing vortices over the double-delta wing configuration as the angle of attack is increased is of interest to flight of modern fighter aircraft at high angle of attack. The scope of this investigation is to explore the ability of a second-order accurate in-space computational method in resolving the flowfield over the double-delta wing. Solutions over the delta wing for fixed angles of incidence and for oscillatory motion have been obtained with a third-order, upwind-biased scheme in Ref. 11, where the unsteady flowfield is investigated.

Experimental work by Cunningham and den Boer[6] focused on the study of the vortical flowfield over a double-delta (strake-delta) wing configuration. A rich variety of flow regimes is observed over this double-delta wing configuration as the angle of attack is increased. At low angles of attack, leading-edge vortices from both the strake and wing are present, but remain separated. As the angle of attack increases, the strake and wing vortices start to interact. The experimental study of Ref. 6 investigated both flows at fixed angles of attack and the unsteady flow response resulting from forced oscillatory motion of the wing surface. The objective of the present numerical study is to investigate in detail the structure of the flowfield over the double-delta wing configuration at various fixed angles of attack. Flow phenomena, including interaction of the strake and wing vortices and vortex breakdown are examined in detail in the computed solutions and are validated through comparison with the experimental measurements of Ref. 6.

Computational Method

Governing Equations

The thin-layer compressible Navier-Stokes equations were used to obtain the numerical solution. The strong conservation-law form of the governing equations for a curvilinear coordinate system (ξ, η, ζ) along the axial, circumferential, and normal directions, respectively, is as follows:

$$\partial_t \hat{\boldsymbol{Q}} + \partial_\xi \hat{\boldsymbol{F}} + \partial_\eta \hat{\boldsymbol{G}} + \partial_\zeta \hat{\boldsymbol{H}} = Re^{-1} \partial_\zeta \hat{\boldsymbol{S}} \tag{1}$$

where $\hat{\boldsymbol{Q}}$, $\hat{\boldsymbol{F}}$, $\hat{\boldsymbol{G}}$, $\hat{\boldsymbol{H}}$ are

$$\hat{\boldsymbol{Q}} = \frac{1}{J}\begin{bmatrix} \rho \\ \rho u \\ \rho v \\ \rho w \\ e \end{bmatrix}, \qquad \hat{\boldsymbol{F}} = \frac{1}{J}\begin{bmatrix} \rho U \\ \rho u U + \xi_x p \\ \rho v U + \xi_y p \\ \rho w U + \xi_z p \\ (e + p)U - \xi_t p \end{bmatrix}$$

$$\hat{\boldsymbol{G}} = \frac{1}{J}\begin{bmatrix} \rho V \\ \rho u V + \eta_x p \\ \rho v V + \eta_y p \\ \rho w V + \eta_z p \\ (e + p)V - \eta_t p \end{bmatrix}, \qquad \hat{\boldsymbol{H}} = \frac{1}{J}\begin{bmatrix} \rho W \\ \rho u W + \zeta_x p \\ \rho v W + \zeta_y p \\ \rho w W + \zeta_z p \\ (e + p)W - \zeta_t p \end{bmatrix}$$

$$\hat{\boldsymbol{S}} = \frac{1}{J}\begin{bmatrix} 0 \\ \mu m_1 u_\zeta + (\mu/3) m_2 \zeta_x \\ \mu m_1 v_\zeta + (\mu/3) m_2 \zeta_y \\ \mu m_1 w_\zeta + (\mu/3) m_2 \zeta_z \\ \mu m_1 m_3 + (\mu/3) m_2 + (\zeta_x u + \zeta_y v + \zeta_z w) \end{bmatrix}$$

Here

$$m_1 = \zeta_x^2 + \zeta_y^2 + \zeta_z^2, \qquad m_2 = \zeta_x u_\zeta + \zeta_y v_\zeta + \zeta_z w_\zeta$$

$$m_3 = (u^2 + v^2 + w^2)/2 + \kappa Pr^{-1} \left(\frac{\partial a^2}{\partial \zeta} \right)$$

and U, V, and W are the contravariant velocity components given by $U = u\xi_x + v\xi_y + w\xi_z + \xi_t$, etc. In the above equations all geometrical dimensions are normalized with the wing-root chord length; ρ is the density normalized with the freestream density ρ_∞; u, v, and w are the Cartesian velocity components of the physical domain normalized with the freestream speed of sound a_∞; e is the total energy per unit volume normalized with $\rho_\infty a_\infty^2$; Pr is the Prandtl number; and κ is the thermal conductivity. The pressure is related to density and total energy through the equation of state for an ideal gas, $p = (\gamma - 1)[e - \rho(u^2 + v^2 + w^2)/2]$.

Numerical Implementation

The numerical integration is performed using a partially flux-split[12] numerical scheme. The upwinding is performed in the main flow direction with flux-vector splitting, and central differencing is used in the other two spatial directions. The resulting two-factored algorithm is

$$\begin{aligned} &[I + h\delta_\xi^b (A^+)^n + h\delta_\zeta C^n - hRe^{-1}\bar{\delta}_\zeta J\ {}^1M^n J - D_{i|\zeta}] \\ &\quad \times [I + h\delta_\xi^f (A^-)^n + h\delta_\eta B^n - D_{i|\eta}]\Delta q^n \\ &\quad = -\Delta t\{\delta_\xi^b[(F^+)^n - F_\infty^n] + \delta_\xi^f[(F^-)^n - F_\infty^n] \\ &\quad + \delta_\eta(G^n - G_\infty) + \delta_\zeta(H^n - H_\infty) \\ &\quad + Re^{-1}\delta_\zeta(S^n - S_\infty)\} - D_e(q^n - q_\infty) \end{aligned} \tag{2}$$

In Eq. (2) D_e denotes the explicit dissipation terms that are used along the directions where central differencing is employed, and D_i denotes the implicit dissipation terms that are added for numerical stability. The dissipation terms used are a combination of second- and fourth-order terms. The fourth-order terms provide background damping of the high-frequency modes. The second-order terms are used to control the oscillation in the neighborhood of shock waves, and are turned on when strong pressure gradients are sensed in the flow. The implicit and explicit dissipation terms are computed as suggested in Ref. 13.

In the experiment reported in Ref. 6, the Reynolds number based on the wing-root chord length is high enough ($Re_c = 4.0 \times 10^6$) to expect the flow to be mostly turbulent over most of the wing surface. Transitional flow is expected to have an effect only in the regions very close to the apex of the wing. Present knowledge about transition does not enable computation and modeling of the transitional regime. Therefore, only fully turbulent solutions were computed. The Baldwin-Lomax eddy viscosity model[14] as modified by Degani and Schiff[15] for the computation of separated vortical flows was used.

The strake-delta wing configuration of Ref. 6 was used for the numerical simulation. It consists of a sharp leading-edge, 76-deg sweep strake of diamond cross section, connected to a 40-deg sweep wing section formed by NACA 64A005 sections. The surface geometry can be defined algebraically. Figure 1a shows the grid topology and the surface grid where the wing dimensions are normalized by the root chord. Only half-body solutions are computed and reflection boundary conditions are applied at the symmetry plane. These solutions were obtained on a spherical or C-O grid topology that has a singular line on the wing apex and O-type grid planes at each circumferential $\eta - \zeta$ cross section. Figure 1b shows the C-type topology along the streamwise direction for the $\xi - \zeta$ grid planes that originate from the singular axis at the wing apex. Previous investigations[16,17] have shown that the spherical grid topology provides an efficient distribution of grid points over delta wings and enables grid orthogonality at the wing leading edge for low sweep angle delta wings. The grid boundaries were placed approximately 2.5 root chord lengths away from the wing surface. Clustering was used in the normal direction to enable capturing of the surface viscous layers. The distance of the first point from the wing surface was

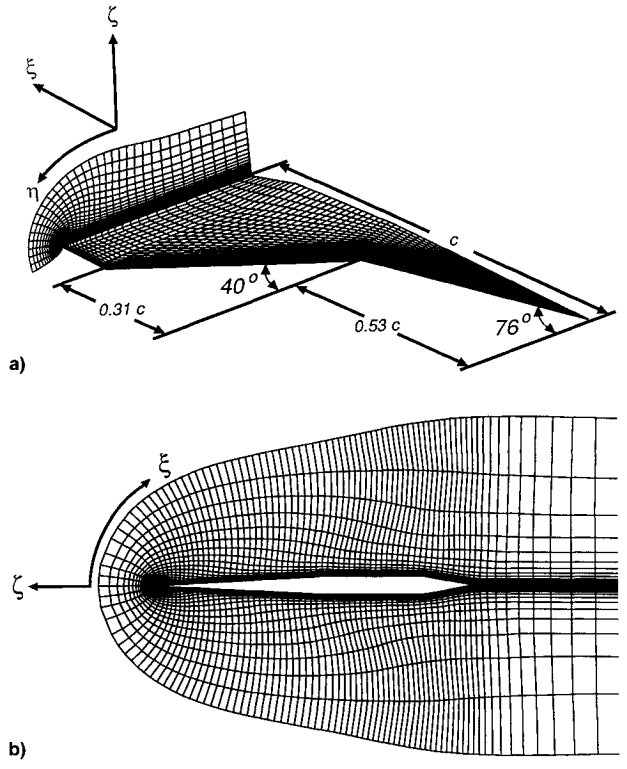

Fig. 1 Surface grid and double-delta wing dimensions.

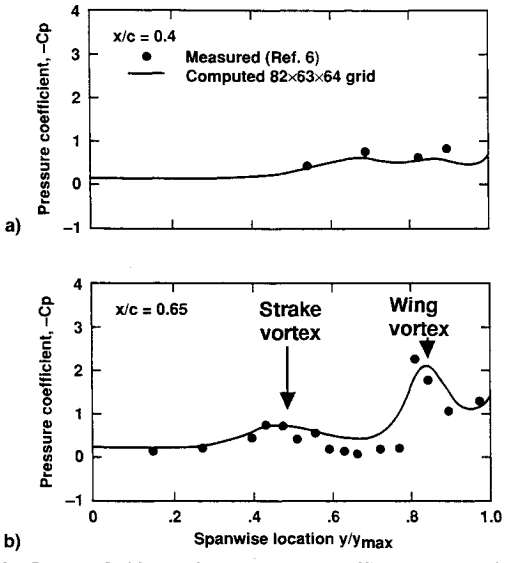

Fig. 2 Leeward-side surface pressure coefficient; $M = 0.22$, $\alpha = 10.0$ deg, $Re = 4.0 \times 10^6$ (turbulent).

0.00001 chord lengths. An 82 × 63 × 64 point grid along the streamwise or ξ, circumferential or η, and normal or ζ directions, respectively, was used as a baseline grid. Grid refinement studies were done with an 82 × 117 × 64 point grid having increased resolution in the circumferential direction. Solutions were performed in a time-accurate manner and convergence of three orders of magnitude of the residuals was achieved. The solutions were run on the Cray Y-MP and a typical solution was obtained in approximately 30 CPU hours.

Results and Discussion

Computations were carried out for flow conditions matching the experimental conditions of Ref. 6. The freestream Mach number was $M_\infty = 0.22$, and the Reynolds number based on the root chord length was $Re_c = 4.0 \times 10^6$. Solutions were obtained for angles of attack $\alpha = 10$, 19, and 22.4 deg. All solutions were computed as fully turbulent using the Baldwin-Lomax[14] eddy viscosity model, as modified by Degani and Schiff.[15] For the lower angle of attack case $\alpha = 10$ deg, the strake and wing vortices did not merge and no vortex breakdown was developed. At the two higher angles of attack, $\alpha = 19$ and 22.4 deg, the computation, as well as the flow visualization studies of Ref. 6, showed vortex merging and development of vortex breakdown. At $\alpha = 19$ deg, the two vortices merged at the trailing edge and vortex breakdown was found above the wing surface. At $\alpha = 22.4$ deg, vortex merging and breakdown occurred further upstream. In the following sections the three computed flow cases are discussed in more detail.

Flow at $\alpha = 10.0$ Deg

The solution for $\alpha = 10$ deg was computed on a single-block, spherical, 82 × 63 × 64 point grid. The computed and measured surface pressure coefficients on the strake section ($x/c = 0.4$), and on the wing section ($x/c = 0.65$) are compared in Figs. 2a and 2b, respectively. The location and the strength of the suction peak caused by the primary vortex on the strake section (Fig. 2a) is captured reasonably well by the numerical solution. On the wing section (Fig. 2b) the strength and the location of the suction peak caused by the strake vortex is also predicted closely. However, the pressures induced by the wing vortex are slightly underpredicted, and the spanwise position of the suction peak caused by the primary vortex is found to be located slightly further outboard of the experimental results. Overall, the comparisons of the predicted surface pressure with the measurements suggest that for this angle of attack the strength of the strake and wing vortices are predicted reasonably well. As a result no grid refinement was carried out for this angle of attack.

The flow pattern and the location of the separation and attachment points in a crossflow plane can be identified using the helicity density.[18] The helicity defined as $H = \boldsymbol{V} \cdot \boldsymbol{\omega}$ is a scalar and shows the primary vortex center as the location of helicity maximum in the flowfield, as well as the location of the secondary vortices and secondary separation and attachment by the change of helicity density sign. The helicity density contour plot in a crossflow plane on the strake at $x/c = 0.5$ is shown in Fig. 3a. The primary vortex center is the location where the helicity density attains its maximum value. The secondary vortex and the separation and attachment point in the crossflow plane are identified under the primary vortex by the negative helicity density values indicated by dashed line. A second sign reversal of the helicity density close to the symmetry plane suggests crossflow reversal outboard of the symmetry plane. The schematic of Fig. 3b shows the streamline flow pattern corresponding to the computed helicity contours in the crossflow plane at $x/c = 0.5$. The computed surface flow patterns and crossflow field information similar to the one shown in Fig. 3a are used to draw the schematic of Fig. 3b. In Fig. 3b the primary and the secondary separation and attachment points are indicated as S_1, S_2 and A_1, A_2, respectively, and the separation at the centerline is indicated as S. This streamline pattern satisfies the topological rules governing the behavior of the flow in a crossflow plane given in Ref. 19. The skin-friction line passing through the attachment point A_2 starts from the apex as the approximately conically symmetric structure of the strake flowfield would require.

At the junction of the strake with the wing the strake vortex continues propagating over the wing flowfield, causing flow separation. Observation of the surface flow, however, indicates that the strake vortex lifts off the wing surface. The helicity density contour plot in a crossflow plane at $x/c = 0.85$ (Fig. 4a) shows both the primary wing vortex and the trace of the strake vortex. The streamline flow pattern in this crossflow plane is shown schematically in Fig. 4b. The secondary separation started on the strake is maintained by the combined

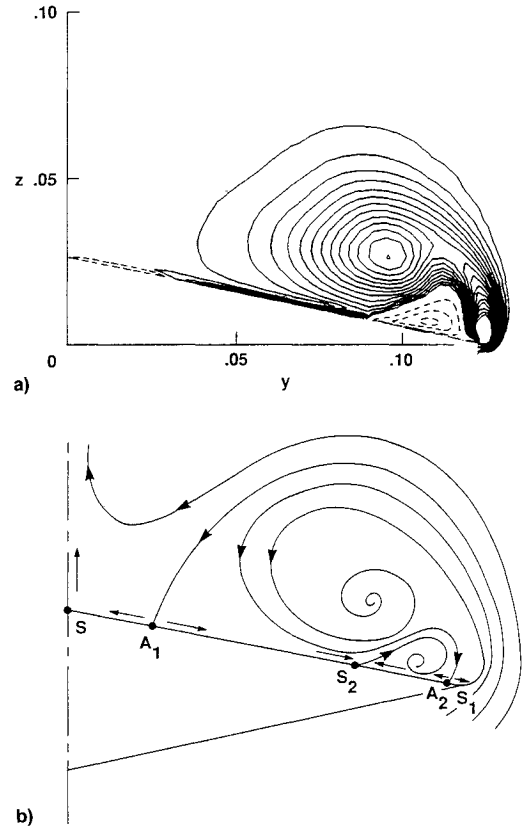

Fig. 3 Helicity density contours and schematic streamline pattern in a crossflow plane at $x/c = 0.50$; $M = 0.22$, $\alpha = 10$ deg, $Re = 4.0 \times 10^6$ (turbulent).

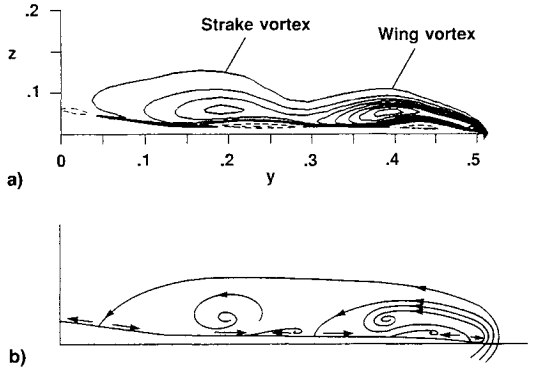

Fig. 4 Helicity density contours and schematic streamline pattern in a crossflow plane at $x/c = 0.85$; $M = 0.22$, $\alpha = 10$ deg, $Re = 4.0 \times 10^6$ (turbulent).

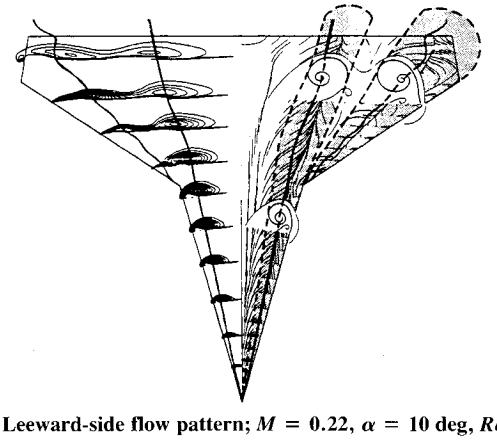

Fig. 5 Leeward-side flow pattern; $M = 0.22$, $\alpha = 10$ deg, $Re = 4.0 \times 10^6$ (turbulent).

action of the strake and wing vortices, while the attachment of the flow separated from the leading edge still occurs outboard of the symmetry line. A global view of the leeward-side flow pattern is shown in perspective view in Fig. 5. On the left, the helicity density contours in crossflow planes at several axial locations are shown. The strake and wing vortex trajectories pass through the centers of the vortices identified by the helicity density contours. On the right, the computed surface flow pattern and the leading-edge vortices are shown. A schematic of the crossflow pattern at two representative locations, one on the strake and the other on the wing, are also sketched. The secondary separation is located approximately under the vortex center on the strake section. On the wing section both the separation and the attachment skin-friction lines that originated at the strake have been moved further outboard due to interaction with the vortical flowfield caused by the wing vortex. The strake and wing vortices remain distinct over the wing surface for flow at $\alpha = 10$ deg.

Flow at $\alpha = 19.0$ Deg

The solution at $\alpha = 19.0$ deg was computed on a single-block, spherical, $82 \times 63 \times 64$ point grid, and on a $82 \times 117 \times 64$ point grid that provides increased resolution in the circumferential direction. The computed and measured surface pressure coefficients at $x/c = 0.4$ and 0.65 are compared in Figs. 6a and 6b, respectively, where the predictions on the coarser grid are indicated with dashed line. The suction peak caused by the primary vortex on the strake section (Fig. 6a) is slightly underpredicted by the numerical solution. On the wing section (Fig. 6b) the location of the suction peaks caused by the strake and the wing vortices is predicted reasonably closely. At $x/c = 0.65$, the strength of the strake vortex suction peak is underpredicted by both solutions. The wing vortex suction peak is closely predicted by the solution computed on the circumferentially refined grid. The surface pressure distribution predicted by the coarse grid solution, even though it follows the experimental trends, differs significantly from the measured values between the two suction peaks.

The computed leeward-side off surface vortical flow structure is shown in Fig. 7 with particle traces released from the leading edges of the strake and the wing. Figure 7a shows a top view of the vortex trajectories, and Fig. 7b shows the corresponding side view. The two vortices remain distinct over most of the wing surface. Over the wing the path of the strake vortex initially deflects outboard and towards the wing surface. At the trailing-edge region the two vortices seem to merge, and the wing vortex undergoes breakdown. Vortex breakdown is identified at the location where the velocity in

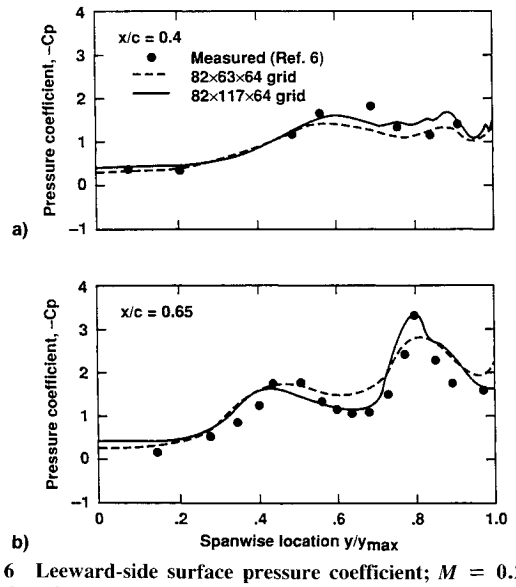

Fig. 6 Leeward-side surface pressure coefficient; $M = 0.22$, $\alpha = 19.0$ deg, $Re = 4.0 \times 10^6$ (turbulent).

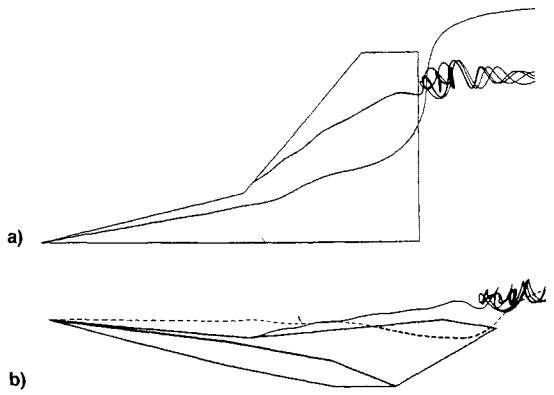

Fig. 7 Leeward-side flow structure; $M = 0.22$, $\alpha = 19$ deg, $Re = 4.0 \times 10^6$ (turbulent).

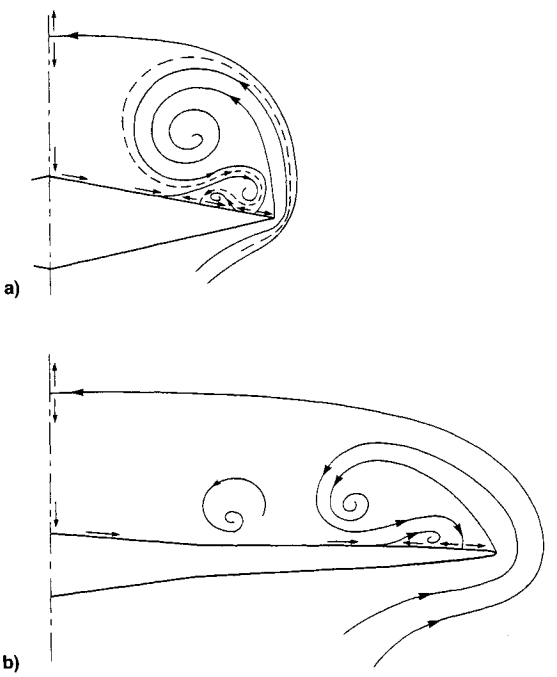

Fig. 8 Streamline flow pattern in crossflow planes on a) the strake and b) the wing.

the vortex core decreases and the core enlarges. For $\alpha = 19$ deg the wing vortex is found further inboard from the wing leading edge than occurs in the $\alpha = 10$-deg case. As a result, the strake and wing vortices interact more strongly and finally merge further downstream. The strake vortex follows an S-shape trajectory, clearly shown in the top view of Fig. 7a. The strake vortex is initially at a greater distance from the surface. Interaction with the wing vortex causes deflection of its path towards the wing surface and, after merging, particles originated from the strake leading edge at the apex are swept beneath the wing vortex.

A representative crossflow pattern on the strake is shown schematically in Fig. 8a, where the secondary and tertiary separation and attachment lines are indicated. The crossflow pattern on the wing for $x/c \leq 0.8$, in the region where the strake and wing vortices are distinct (Fig. 8), is shown schematically in Fig. 8b. Over the wing the strake vortex is lifted off far enough from the surface and the secondary separation is suppressed. A secondary separation caused by the wing vortex is found close to the wing leading edge. Figure 9 shows a global perspective view of the strake and wing primary vortices and the corresponding surface flow pattern. On the left, the helicity contours and the vortex trajectories are shown.

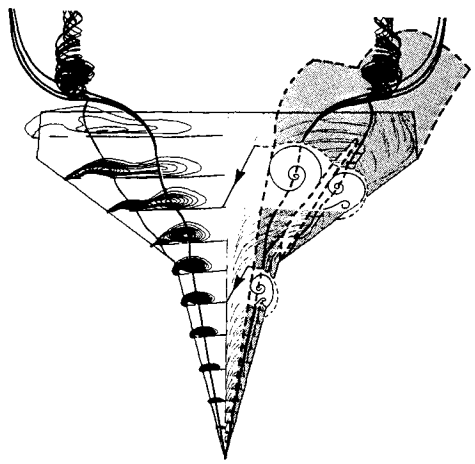

Fig. 9 Leeward-side flow pattern; $M = 0.22$, $\alpha = 19$ deg, $Re = 4.0 \times 10^6$ (turbulent).

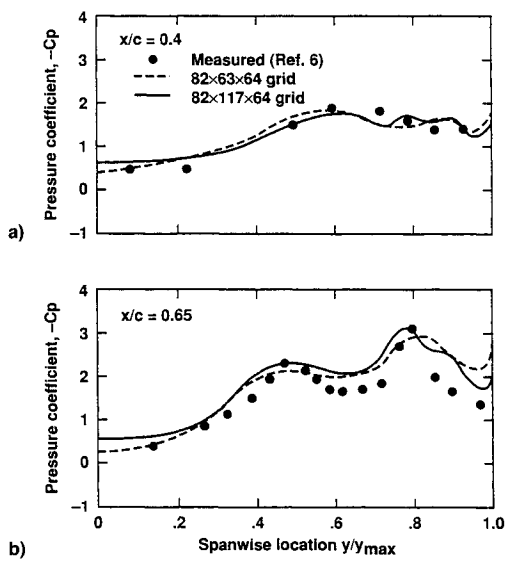

Fig. 10 Leeward-side surface pressure coefficient; $M = 0.22$, $\alpha = 22.4$ deg, $Re = 4.0 \times 10^6$ (turbulent).

On the right, the surface flow pattern and the crossflow pattern in two representative crossflow planes over the strake and the wing, respectively, are shown. The strake and wing vortices sketched with dashed line indicate the merging in the trailing-edge region.

Flow at $\alpha = 22.4$ Deg

The solution at $\alpha = 22.4$ deg was also computed on a single-block, spherical, $82 \times 63 \times 64$ point grid, and on a $82 \times 117 \times 64$ point grid that provides increased resolution in the circumferential direction. The computed and measured surface pressure coefficients at $x/c = 0.4$ and 0.65 are compared in Figs. 10a and 10b, respectively. The surface pressure predictions obtained from the coarser grid solution are indicated with a dashed line. The suction peak caused by the primary vortex on the strake section (Fig. 10a) is slightly underpredicted by the numerical solution. On the wing section (Fig. 10b) the location and strength of the suction peaks caused by the strake and the wing vortices are predicted closely. However, the surface pressure distribution predicted by both solutions, even though it follows the experimental trends, differs significantly from the measured values between the two suction peaks.

The computed leeward-side off-surface vortical flow structure is shown in Fig. 11 with particle traces released from the strake and wing leading edges. Figure 11a shows a top view

of the vortex trajectories, and Fig. 11b shows the corresponding side view. The two vortices remain distinct over a smaller portion of the wing surface compared to the α = 19-deg case. A larger deflection of the strake vortex path outboard towards the wing leading edge and towards the wing surface is observed. The two vortices merge above the wing upstream of the trailing edge, and the wing vortex suffers breakdown. The breakdown region has a larger extent compared to the α = 19-deg case. The strake vortex again follows an S-shape path, which is clearly shown in the top view of Fig. 11a. Observations of the computed flowfield indicate that at α = 22.4 deg, vortex merging occurs at $x/c \approx 0.75$. The global strake and wing vortex system and the corresponding flow pattern are similar to the one shown in Fig. 9.

A perspective view of the computed leeward side vortical flowfields at α = 19 and 22.4 deg is shown in Fig. 12. Total pressure contours at several crossflow planes are used to demonstrate the development of the vortical flowfield. The paths of the vortex cores are indicated by particle traces released from the leading edges of the strake and the wing. The flow at α = 19 deg, shown on the left of Fig. 12, indicates that the two vortices merge in the trailing-edge region. At α = 22.4 deg, vortex merging occurs further upstream and a larger breakdown region is observed.

Vortical Flowfield Analysis

The strake and wing leading-edge vortices consist of fluid elements undergoing spiraling motion about axes defined by the vortex centers. On the wing section, where a two-vortex system exists, mutual interaction of the velocity-vorticity fields is expected to alter the structure of the vortices. It is, therefore, instructive to study the variation of the flow quantities, such as the velocity magnitude, along the vortex trajectories in order to better understand the structure of the flowfield.

The velocity magnitude is obtained from spatial interpolation of the computed flowfield for points located on the strake and wing vortex trajectories. The variation of the velocity magnitude, nondimensionalized by the freestream speed, along these vortex trajectories for α = 10 deg, is shown in Fig. 13. In the strake vortex, after a rapid initial rise, the velocity magnitude increases gradually along the vortex until the junction with the wing is reached. Beyond this point the velocity magnitude decreases monotonically. The wing vortex velocity magnitude initially increases and then decreases monotonically, showing an increase of magnitude downstream of the wing trailing edge. The decrease of the velocity along the wing vortex, after a short distance from the wing-strake junction, is due to the influence of the cropped wingtip and wing trailing edge. The variation of the velocity magnitude along the vortex trajectory for α = 19 and 22.4 deg, where stronger vortex interaction was observed, is shown in Figs. 14 and 15, respectively. The variation of the velocity magnitude along the wing vortex shows a similar behavior to the α = 10-deg case. Here, the location of the local extremum in wing vortex velocity magnitude is closely associated with the location of

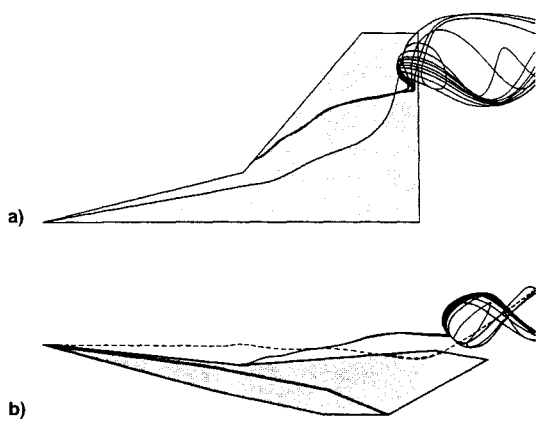

Fig. 11 Leeward-side flow structure; M = 0.22, α = 22.4 deg, Re = 4.0 × 10⁶ (turbulent).

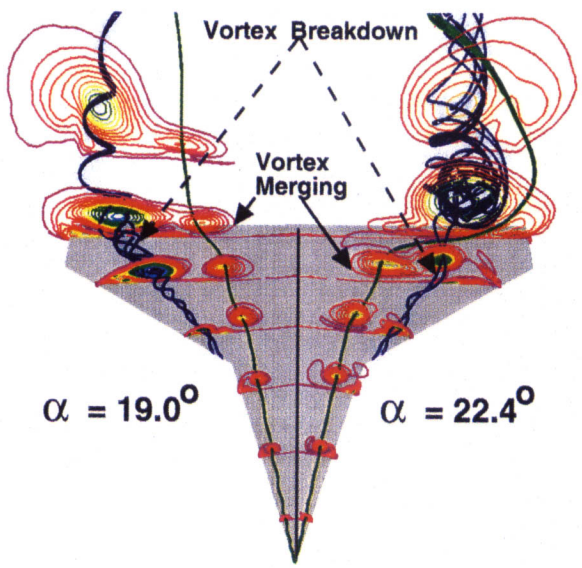

Fig. 12 Leeward-side vortical flowfield shown with total pressure contours; M = 0.22, α = 19 and 22.4 deg, Re = 4.0 × 10⁶ (turbulent).

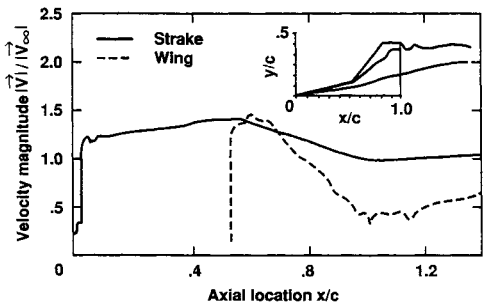

Fig. 13 Variation of nondimensional velocity V/V_∞ along the strake and wing vortex trajectories at α = 10.0 deg.

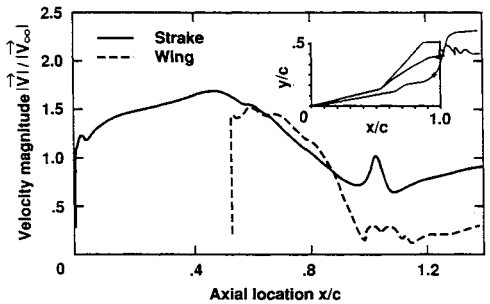

Fig. 14 Variation of nondimensional velocity V/V_∞ along the strake and wing vortex trajectories at α = 19.0 deg.

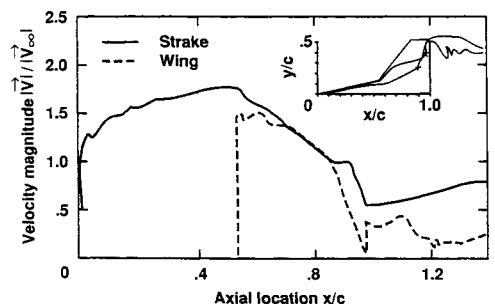

Fig. 15 Variation of nondimensional velocity V/V_∞ along the strake and wing vortex trajectories at α = 22.4 deg.

vortex breakdown along the wing vortex. However, the behavior of the velocity magnitude along the strake vortex at $\alpha = 19$ and 22.4 deg is quite different from the behavior observed for the $\alpha = 10$-deg case. The velocity magnitude along the strake vortex is decreasing after the junction with the wing, and increases downstream of the wing trailing edge, showing a local extremum at the trailing-edge region. The location of the local extrema is marked on the vortex trajectories in Figs. 14 and 15.

Summary

The flow over a strake delta wing configuration was investigated by the numerical solution of the thin-layer compressible Navier-Stokes equations. The computed solution for $\alpha = 10$ deg shows reasonable agreement with the experimental measurements. At this angle of attack, the strake and wing vortices do not interact strongly, and remain separate over the wing. The computed solutions at higher angles of attack, $\alpha = 19$ and 22.4 deg, are again in reasonable agreement with the experimental measurements. Grid refinement in the circumferential direction improved the agreement between computed and measured surface pressure distributions. Vortex interaction and merging of the strake and wing vortices was found for the two higher angle-of-attack cases. After merging, the vortices suffer vortex breakdown, and the breakdown location was found to move further upstream with increasing angle of attack. Further studies of the effects of the solution procedure and grid resolution are required in order to better ascertain the validity of the present results.

Acknowledgment

The support of this investigation by the Naval Postgraduate School Internal Research Program is gratefully acknowledged.

References

[1]Faler, J. H., and Leibovich, S., "Disrupted States of Vortex Flow and Vortex Breakdown," *Physics of Fluids*, Vol. 20, No. 9, 1977, pp. 1385–1400.

[2]Payne, F. M., and Nelson, R. C., "An Experimental Investigation of Vortex Breakdown on Delta Wings," *Vortex Flow Aerodynamics*, NASA CP-2416, 1985, pp. 135–161.

[3]Kjelgaard, O., and Sellers, W. L., "Detailed Flowfield Measurements over a 75° Swept Delta Wing for Code Validation," AGARD Symposium on Validation of CFD, Lisbon, Portugal, May, 1988.

[4]Magness, C., Robinson, O., and Rockwell, D., "Control of Leading-Edge Vortices on a Delta Wing," AIAA Paper 89-0999, March 1989.

[5]Roos, F. W., and Kegelman, J. T., "An Experimental Investigation of Sweep-Angle Influence on Delta Wing Flows," AIAA Paper 90-0383, Jan. 1990.

[6]Cunningham, A. M., and Den Boer, R. G., "Low-Speed Unsteady Aerodynamics of a Pitching Strake Wing at High Incidence—Part II: Harmonic Analysis," *Journal of Aircraft*, Vol. 27, No. 1, 1990, pp. 31–41.

[7]Fujii, K., and Schiff, L. B., "Numerical Simulation of Vortical Flows over Strake-Delta Wing," *AIAA Journal*, Vol. 27, No. 9, 1989, pp. 1153–1162.

[8]Thomas, J. L., Krist, S. T., and Anderson, W. K., "Navier-Stokes Computations of Vortical Flows over Low-Aspect-Ratio Wings," *AIAA Journal*, Vol. 28, No. 2, 1990, pp. 205–212.

[9]Kandil, O. A., and Chuang, A. H., "Unsteady Vortex-Dominated Flows Around Maneuvering Wings over a Wide Range of Mach Numbers," AIAA Paper 88-0317, Jan. 1988.

[10]Hsu, C. H., and Liu, C. H., "Prediction of Vortical Flows on Wings Using Incompressible Navier-Stokes Equations," Third International Congress of Fluid Mechanics, Cairo, Egypt, Jan. 1990.

[11]Ekaterinaris, J. A., and Schiff, L. B., "Navier-Stokes Solutions for an Oscillating Double-Delta Wing," AIAA Paper 91-1624, June 1991.

[12]Ying, S. X., Steger, J. L., Schiff, L. B., and Baganoff, D., "Numerical Simulation of Unsteady, Viscous High-Angle-of-Attack Flows Using a Partially Flux-Split Algorithm," AIAA Paper 86-2179, Aug. 1986.

[13]Pulliam, T. H., "Artificial Dissipation Models for the Euler Equations," *AIAA Journal*, Vol. 24, No. 12, 1986, pp. 1931–1940.

[14]Baldwin, B. S., and Lomax, H., "Thin Layer Approximation and Algebraic Model for Separated Turbulent Flows," AIAA Paper 78-275, Jan. 1978.

[15]Degani, D., and Schiff, L. B., "Computation of Turbulent Supersonic Flows Around Pointed Bodies Having Crossflow Separation," *Journal of Computational Physics*, Vol. 66, No. 1, 1986, pp. 173–196.

[16]Ekaterinaris, J. A., and Schiff, L. B., "Numerical Predictions of Vortical Flows over Slender Delta Wings," *Journal of Aircraft*, Vol. 30, No. 6, 1993, pp. 935–942.

[17]Ekaterinaris, J. A., and Schiff, L. B., "Numerical Invstigation of the Effects of Variation of Angle of Attack and Sweep Angle on Vortex Breakdown over Delta Wings," AIAA Paper 90-3000, Aug. 1990.

[18]Levy, Y., Seginer, A., and Degani, D., "Graphical Visualization of Vortical Flows by Means of Helicity," *AIAA Journal*, Vol. 28, No. 8, 1990, pp. 1347–1352.

[19]Tobak, M., and Peake, D. J., "Topology of Three-Dimensional Separated Flows," *Annual Review of Fluid Mechanics*, Vol. 14, 1982, pp. 61–85.